IEEE Access
Multidisciplinary | Rapid Review | Open Access Journal

Received August 10, 2021, accepted August 26, 2021, date of publication August 31, 2021, date of current version September 14, 2021.

Digital Object Identifier 10.1109/ACCESS.2021.3109487

Optimal Design of Functionally Graded Power Cable Joint Utilizing Silicone Rubber/Carbon Nanotube Composites

YIFAN ZHANG[1], YONGJIE NIE[2], BING LUO[1], MINGLI FU[1], (Member, IEEE), SHUAI HOU[1], BAOJUN HUI[1], XIANPING ZHAO[2], BIN FENG[1], AND WENBO ZHU[1]

[1]State Key Laboratory of HVDC, CSG Electric Power Research Institute Co., Ltd., China Southern Power Grid, Guangzhou, Guangdong 510663, China
[2]Electric Power Research Institute, Yunnan Power Grid Co., Ltd., Kunming, Yunnan 650217, China

Corresponding authors: Yifan Zhang (zhangyf@csg.cn) and Yongjie Nie (nieyongjie@163.com)

This work was supported by the Science and Technology Program of China Southern Power Grid under Grant ZBKJXM20180565.

ABSTRACT Functionally graded materials (FGMs) used in electrical insulation have spatially inhomogeneous dielectric properties (i.e., permittivity or conductivity), which can be applied to relieve localized electric field (E-field) intensification and improve insulation performance. However, previous research shows some limitations in inadequate considerations on the material feasibility, and insufficient universality on material grading type and voltage form. In this study, a material study of silicone rubber (SiR) nanocomposites containing carbon nanotubes (CNTs) is conducted to determine the practical variation range of dielectric properties (both permittivity and conductivity) in joint insulation materials. Then, the optimal design of both multilayer and pointwise FGM joint insulation is investigated under both AC and DC voltage, in which the lower and upper limits of permittivity and conductivity were derived from the experimental results. Experimental results on SiR/CNT nanocomposites indicate that low-amount doping of the CNTs (0-0.5% wt%) can effectively increase the permittivity and conductivity of joint insulation materials. The successive simulation study indicates that compared to uniform joints, cable joints employing optimally designed FGM insulation show a considerable increase in the E-field utilization factor (from 0.08-0.17 to 0.23-0.56), indicating elevated E-field uniformity. Finally, the optimal range of CNT doping ratios is determined to be 0-0.3 wt% from both experimental and simulation results. This study systematically verifies the applicability of FGMs in enhancing the performance of power cable accessories, which can show some guidance to the design and fabrication of advanced power cable systems.

INDEX TERMS Dielectric properties, electric field optimization functionally graded material, polymeric nanocomposites power cable insulation.

I. INTRODUCTION

Cross-linked polyethylene (XLPE) cables are widely used in electric power transmission systems, especially in urban and submarine applications where space is limited [1]–[3]. According to service data, the reliability of a power cable system is restricted by cable accessories (joints and terminations) because they have a much higher probability of failure than the cable itself [4]. The vulnerability of cable accessories is strongly correlated to the nonuniform distribution of the internal electric field (E-field). This locally intensified E-field stress can lead to electrical treeing and partial discharge, further causing insulation failure [5], [6].

Conventionally, structural field grading components (e.g. stress cone and connection shielding) were utilized to control the E-field distribution. As shown in Fig. 1, field control components are typically made of semiconductive silicone rubber materials, which serve as voltage grading electrodes. The E-field is restricted to an acceptable level for the surrounding insulation medium by optimizing the structure of the stress cone. Despite their effectiveness in E-field grading, a strong mismatch in permittivity or conductivity between the stress cone and insulation medium (regions A and B in Fig. 1) may become a new source of E-field intensification,

The associate editor coordinating the review of this manuscript and approving it for publication was Hui Ma.

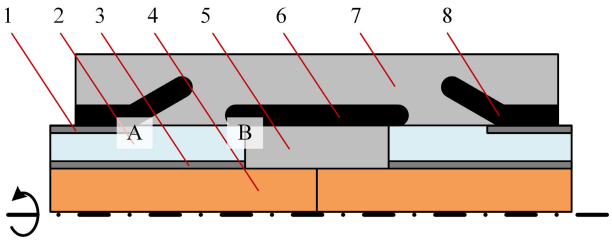

FIGURE 1. Typical structure of a power cable joint, including (1) an outer semiconductive layer, (2) XLPE insulation, (3) an inner semiconductive layer, (4) a cable conductor, (5) a metal connector, (6) connection shielding, (7) joint insulation, and (8) a stress cone.

especially when improper installations or residual impurities are considered [6].

Recently, functionally graded materials (FGMs) have become a promising solution for E-field regulation problems in electrical insulation systems. The FGM is a material system with a spatially nonuniform microstructure and resultant heterogeneous permittivity and/or conductivity [7], [8]. The electric field control problem can be effectively solved by carefully adjusting the spatial distribution of the dielectric properties, resulting in significantly increased dielectric strength with a simplified insulation structure For instance, Kato *et al.* used the centrifugal method to make the FGM spacer which increased the 50% breakdown voltage by 69% in a 0.4MPa SF6 environment [9]. In our previous work [10], we proposed a multilayer 1D FGM cable joint However, some limitations exist in the previous research, including (1) the optimization procedure was conducted under ideal conditions without considering the material feasibility For instance, very high value of maximum permittivity ($\varepsilon_r > 100$) is utilized to realized better E-field regulation performance, which is usually not applicable in practical insulation materials. (2) the effectiveness of other FGM configurations in FGM cable joints, for example, two-dimensional pointwise FGM designed by topology optimization [11], lacks systematic investigation.

In this study, we investigate the applicability of different types of FGMs in power cable joints, in which the material feasibility is experimentally investigated. In section 2, silicone rubber (SiR) material used in cable joints is doped with multiwalled carbon nanotubes (MWCNTs). The purpose of this nano-doping is to adjust the permittivity and conductivity of the SiR insulation. Thereafter, the dielectric properties (relative permittivity, electrical conductivity, dielectric loss, and breakdown strength) and mechanical properties (tensile stress-strain curves, tensile modulus, tensile strength, and elongation at break) of the SiR/MWCNT composites are investigated. In section 3, two types of FGM insulation, including multilayer and pointwise, are used to regulate the E-field distribution under both AC and DC voltages. Finally, the E-field parameters (maximum E-field, E-field stress at certain points, and E-field utilization factor) of the optimized FGM joints are compared in section 4 to judge the applicability of FGM joints in E-field control. We believe that this study can provide conceptual and practical instructions for the development of next-generation, high-reliability, compact-size power cable systems.

II. MATERIALS OF THE FGM CABLE JOINTS

A. MATERIALS AND METHODS

1) RAW MATERIALS

To adjust the permittivity and conductivity of the joint insulation material, the silicone rubber (SiR POWERSIL 737, Wacker Chemie AG) matrix was doped with different amounts of multiwalled carbon nanotubes (MWCNTs, Chengdu Organic Chemicals Co. Ltd.).

The MWCNTs were 2030 nm in diameter and 5002000 nm in length, as shown in the transmission electron microscopic images (TEM, Fig. 2, JEOL, JEM-2100). Prior to usage, a vacuum drying treatment was performed ($<10^{-1}$ Pa, 40 °C, 8 h) on the SiR matrix. MWCNTs were ball-milled in a N_2 atmosphere for 10 h to break the aggregated particles and dried (60 °C 24 h in vacuum) to eliminate residual moisture.

2) FABRICATION OF SiR/MWCNT SPECIMENS

As illustrated in Fig. 3, the SiR/MWCNT specimens were prepared according to the following steps.

(1) Material mixing: The two components (A and B A:B = 1:1 in weight) of the SiR matrix were mixed using a three-roll milling machine. During the milling process, a certain amount of the MWCNT filler was added to the silicone material. The three-rolling procedure lasted for 60–90 min to

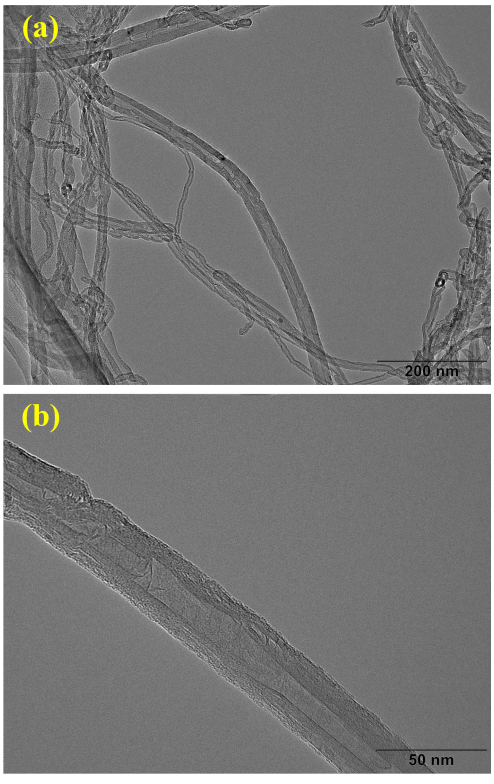

FIGURE 2. TEM images of (a) the MWCNTs and (b) a local magnification.

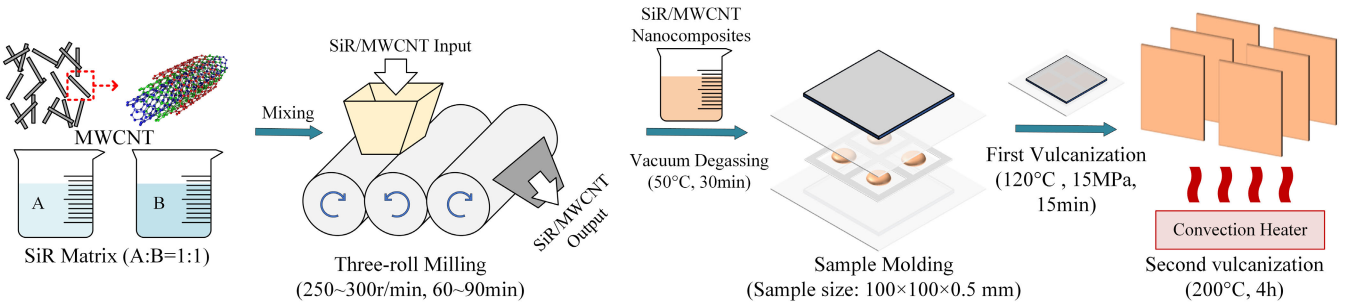

FIGURE 3. Schematic illustration of the preparation of the SiR-*x*CNT specimens.

fully mix the raw materials and promote uniform dispersion of the MWCNT nanofiller in the SiR matrix.

(2) Degassing and molding: The resultant SiR/MWCNT mixture from step 1 was degassed in vacuum for 30 min to eliminate internal bubbles. During the degassing process, the ambient temperature was increased to 50 °C. This was done to decrease the rubber viscosity and promote the de-bubbling process. The degassed rubber was placed in a stainless-steel hot-pressing mold for further vulcanization treatments.

(3) Two-step vulcanization: The first vulcanization was conducted using a hot-pressing device at 120 °C under 15 MPa pressure for 15 min. Then, a second vulcanization was performed at 200 °C for 4 h, leading to better mechanical and insulation performance. The resultant SiR/MWCNT nanocomposites were named SiR-*x*CNT, where *x* is the percentile weight fraction of the MWCNT filler.

3) CHARACTERIZATION

The cross-sectional microstructure of the SiR-*x*CNT composites was observed using scanning electron microscopy (SEM, VE9800S, KEYENCE). Prior to SEM observation, the specimens were cryogenically fractured in liquid N_2, and the cross-sections were sputtered with Au to avoid charge accumulation. During SEM observation, the electron acceleration voltage was 15 kV.

The dielectric properties (dielectric constant ε_r, dielectric loss tanδ, volume conductivity σ_v, and breakdown strength E_b) of the SiR-*x*CNT specimens were characterized on the prepared rubber sheets (100 × 100 × 0.5 mm). Specifically, ε_r and tanδ were measured by a Schering bridge (2821HA, Tettex, Switzerland) shown in Fig 19. σ_v (S/m) was tested using an electrometer (6517 B, Keithley, USA) with an 8009 test fixture (compatible with ASTM D257) under a 500 V DC voltage, as shown in Fig. 20. The dielectric property tests were repeated five times for each specimen

E_b was evaluated use the experimental setup in Fig. 21. The breakdown test was conducted under AC voltage, in which the voltage increased at a rate of 1 kV/s until breakdown occurred. For each type of specimen, the E_b test was repeated more than 15 times, and two-parameter Weibull statistics [12] were used to analyze the data.

The tensile properties were tested according to the ISO 527 standard. During the tensile tests, the stress-strain curves tensile strength (MPa), tensile modulus (MPa), and elongation at break (%) were recorded. Dumb bell-shaped (type 5A, shown in Fig. 4) specimens were cut from the prepared pure SiR or SiR/MWCNT rubber sheets. A universal testing machine (MTS-880/25, USA) was used to conduct the tensile tests. During the test process, the initial distance between the gripping jaws was 20 mm, and the stretching rate was 50 mm/min. The test was repeated 5 times.

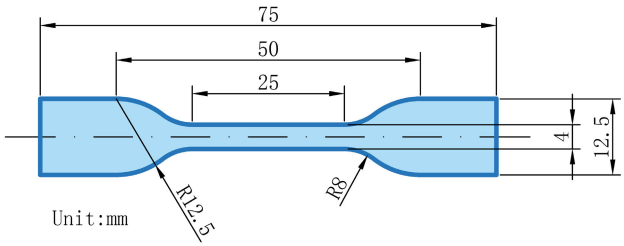

FIGURE 4. Geometric dimensions of type 5A tensile test specimens.

B. DIELECTRIC PROPERTIES

The dielectric constant (ε_r), volume conductivity (σ_v), dielectric loss (tanδ), and breakdown strength (E_b) are shown in Fig. 5. Compared to the pure SiR specimen, SiR-*x*CNT nanocomposites demonstrate a large increase in ε_r and σ_v even if a very low MWCNT doping ratio is employed, e.g., no more than 0.5 wt%. Specifically, the ε_r rises from 2.24 to 15.85 and the σ_v rises from 1.05×10^{-13} S/m to 1.08×10^{-7} S/m.

The rapid increase in ε_r and σ_v can be attributed to the large surface area, high aspect ratio and high conductivity of MWCNTs, which easily induces Maxwell-Wagner-Sillars interfacial polarization and generates percolative conduction paths inside the nanocomposites [13], [14], leading to elevated permittivity and conductivity even at very low doping ratios

However, the presence of MWCNTs in SiR composites may restrict their usage in electrical insulation. From Fig. 5c and 5d, it can be seen that when the MWCNT loading increases from 0 to 0.5 wt%, tanδ rises from 5.24×10^{-4}

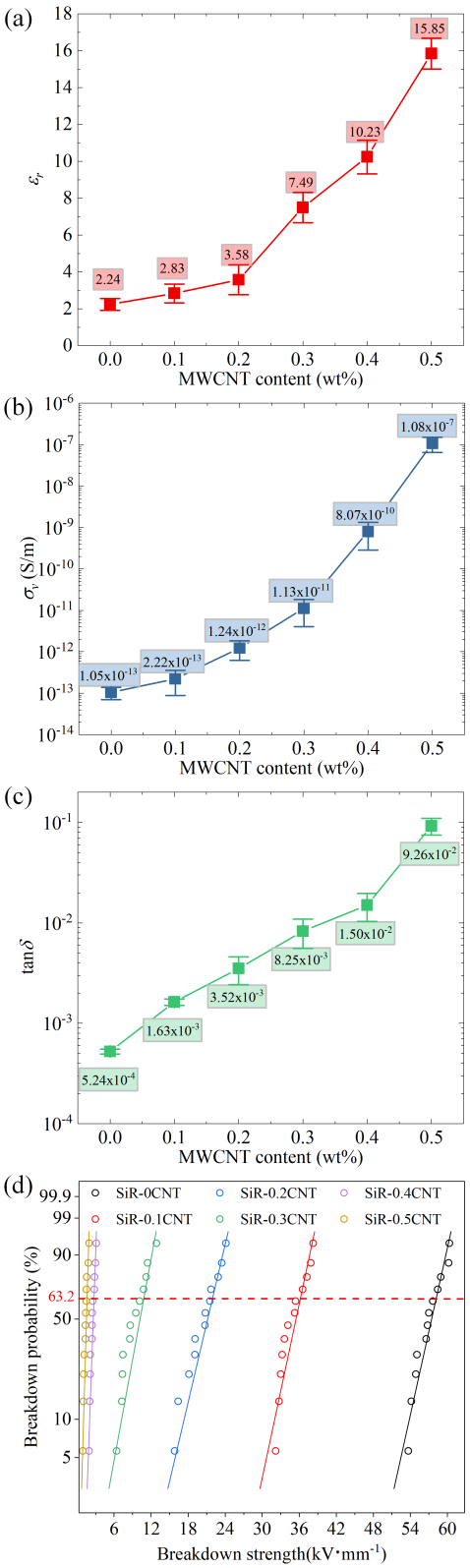

FIGURE 5. Dielectric properties of the SiR-*x*CNT specimens, including (a) dielectric constant, (b) volume conductivity, (c) dielectric loss and (d) Weibull plots of electrical breakdown strength.

to 9.26×10^{-2} and E_b (represented by the Weibull scale parameter, i.e., breakdown E-field strength with 63.2% probability) decreases from 58.01 kV/mm (SiR-0CNT) to 36.39 kV/mm (SiR-0.1CNT), 28.01 kV/mm (SiR-0.2CNT), 10.92 kV/mm (SiR-0.3CNT), 2.83 kV/mm (SiR-0.4CNT) and 1.53 kV/mm (SiR-0.5CNT), indicating dramatic deterioration in the insulation performance.

The large increase in the dielectric loss tanδ is attributed to the rise in conduction loss due to increased σ_v. Moreover, the Maxwell-Wagner-Sillars polarization at the interfaces between the SiR matrix and CNT filler can also increase tanδ [15]. The sharp decrease in breakdown strength E_b is mainly caused by the large difference in conductivity between MWCNTs ($>10^2$ S/cm) and SiR ($<10^{-14}$ S/cm), which induces interfacial electric field intensification and resultant breakdown at the CNT/SiR interfaces [16]. Furthermore, because of the increase in dielectric loss, more heat is generated under the AC field, which increases the possibility of pyrolysis and thermal breakdown [17].

C. MECHANICAL PROPERTIES

Stress–strain curves of the SiR-*x*CNT specimens are shown in Fig. 6a. A linear stress-strain relationship can be observed when the MWCNT loading ratio is no more than 0.3 wt%. At higher loading ratio, deviation from the linear curves exists, and the breakage of specimens occurs earlier.

Tensile modulus E_t, tensile strength σ_t, and elongation at break of the SiR-*x*CNT specimens are depicted in Fig. 6b-d. The tensile modulus remains almost unchanged with the variation of MWCNT contents. The tensile strength and elongation at break both increase when the filling ratio is less than 0.3 wt% and decrease with higher MWCNT contents. In detail, the tensile strength and elongation at break both increases to maximum at 0.3 wt% MWCNT loading, and then decreases with the further increase in the weight fraction of carbon nanotubes. Moreover, the standard deviation is $<10\%$ for all the mechanical properties, indicating good material uniformity of the SiR specimens.

The variation in mechanical properties was correlated to the microstructure of the SiR-*x*CNT nanocomposites shown in Fig. 7. The high-aspect-ratio CNT filler shown in Fig. 7a is similar to glass fiber used in fiber-reinforced plastics (FRPs). Therefore, the existence of the MWCNTs can improve the mechanical strength of SiR-*x*CNT materials, especially when x is less than 0.3. For higher loading ratio, the aggregation of the MWCNT particles (shown in Fig. 7b) can easily occur due the reduction of interparticle distances. These aggregates can lead to decrease in tensile strength and elongation at break due to the mechanical stress concentration and internal microcracks generated at the surface of SiR polymer and aggregated MWCNTs [18].

III. DESIGN OF THE FGM CABLE JOINTS

In this section, the multilayer and pointwise FGM joints, are designed to evaluate their E-field regulation performance. The variation range of the permittivity and conductivity was determined according to experimental data in section 2B.

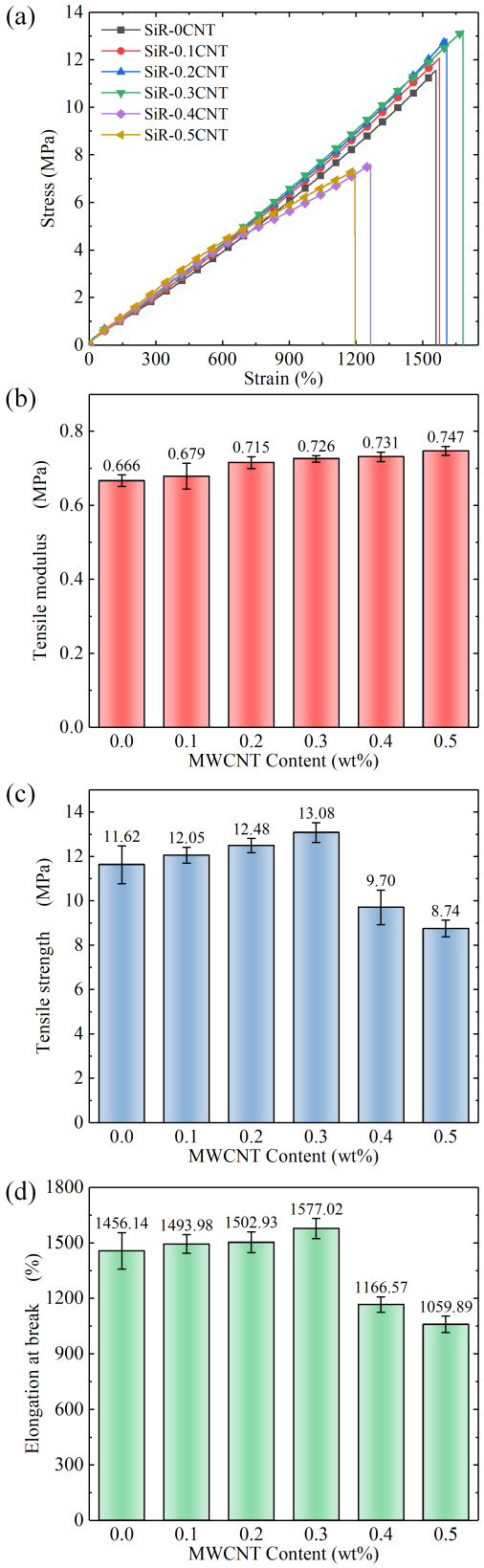

FIGURE 6. Mechanical properties of the SiR-*x*CNT specimens, including (a) stress-strain curves of tensile tests, (b) tensile modulus, (c) tensile strength, and (d) elongation at break.

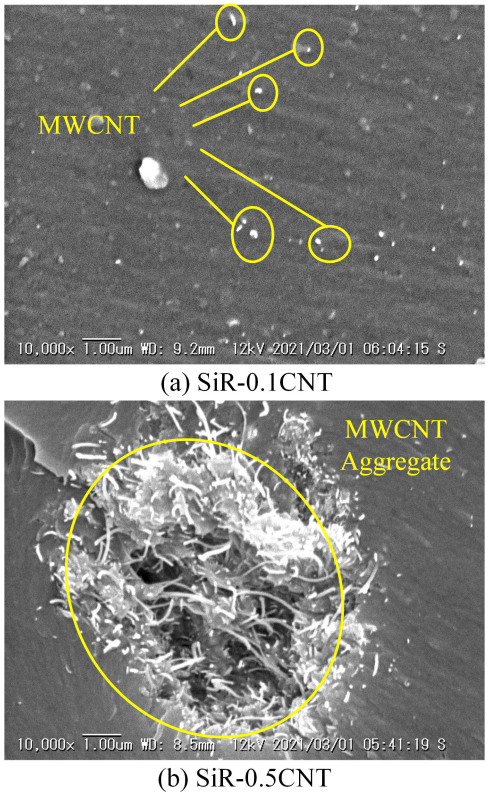

FIGURE 7. Cross-sectional SEM images of (a) SiR-0.1CNT and (b) SiR-0.5CNT.

A. DESIGN METHODS

1) STRUCTURE OF FGM CABLE JOINTS

Fig. 8 shows the structure of studied cable joint, which is identical to a commercially available 110 kV product The innermost parts are two copper conductors, electrified to 110 kV and joined by a metal connector. The metal conductors and the remaining XLPE insulation are wrapped by SiR joint insulation, where the permittivity and conductivity are uniformly equal to the values of the pure SiR material (i.e., SiR-0CNT). The outermost part is the shielding layer connected to the ground.

Structure of FGM joints are shown Fig. 8b-e, four types of power cable joints are taken into consideration:

1) Multilayer permittivity FGM (ε-FGM), in which a radial layered gradient of permittivity is utilized.

2) Pointwise ε-FGM, in which a two-dimensional permittivity gradient is arranged.

3) Multilayer conductivity FGM (σ-FGM) and 4) pointwise σ-FGM, which has similar structure to ε-FGM despite that the conductivity, instead of permittivity, becomes non-uniform.

In this paper, five types of fgm materials were utilized according to the experimental data in fig. 5. the variation range of permittivity and conductivity during the design process is determined by table 1 for instance, in fgm joints

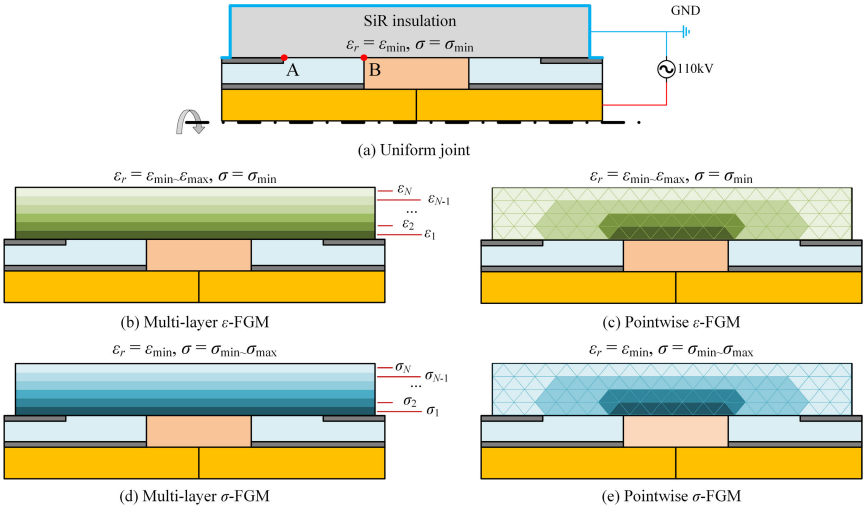

FIGURE 8. Structure of the 110 kV uniform and FGM cable joints.

TABLE 1. Material properties of FGM insulation materials.

Material Name	MWCNT content	Variation range of relative permittivity	Variation range of electrical conductivity, S/m
Uniform	None	Constant: 2.24	Constant: 1.05×10^{-13}
FGM-0.1CNT	0 to 0.1 wt%	2.24 to 2.83	1.05×10^{-13} to 2.22×10^{-13}
FGM-0.2CNT	0 to 0.2 wt%	2.24 to 3.58	1.05×10^{-13} to 1.24×10^{-12}
FGM-0.3CNT	0 to 0.3 wt%	2.24 to 7.49	1.05×10^{-13} to 1.13×10^{-11}
FGM-0.4CNT	0 to 0.4 wt%	2.24 to 10.23	1.05×10^{-13} to 8.07×10^{-10}
FGM-0.5CNT	0 to 0.5 wt%	2.24 to 15.85	1.05×10^{-13} to 1.08×10^{-7}

(regardless of multilayer or pointwise) where fgm-0.3cnt is utilized, the variation range of permittivity (for ε-fgm) and conductivity (for σ-fgm) in each layer or each point are 2.24 to 7.49 and 1.05×10^{-13} to 1.13×10^{-11} s/m, respectively. The actual values of material's permittivity and conductivity in different layers or points are independent to each other, and were determined by the design process. hereafter, a spatially non-uniform permittivity or conductivity is realized and fgm joint structure is built.

2) CALCULATION OF ELECTRIC FIELD DISTRIBUTION

Finite element method (FEM) was employed to calculate the E-field distribution using COMSOL software. The dielectric properties of the cable joint parts were determined according to Table 2 The FEM calculation was conducted under 50 Hz AC voltage for ε-FGM joints and DC voltage for σ-FGM joints. During the calculation, the resolution of the triangular meshing is increased in the vicinity of regions A and B, leading to higher numerical accuracy (Fig. 9a). When the

TABLE 2. Material properties used in FEM simulation.

Material	Dielectric constant, ε_r	Conductivity σ, S/m
Conductors	1.00×10^{6}	5.70×10^{7}
Semi-Conductive Layer *	3500	1.50
XLPE Insulation	2.30	1.00×10^{-14}
Joint Insulation	Shown in Table I	

* According to [10].

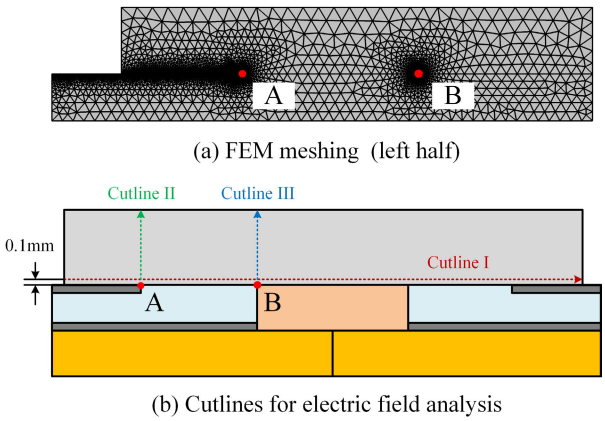

FIGURE 9. Meshing and cutline arrangement in the FEM calculation.

FEM calculation was completed, the E-field contour and E-field magnitude along three cutting lines in Fig. 9b were extracted. In detail, cutline I represents the field distribution along the inner interface of the SiR and XLPE cables, while cutting lines II and III indicate the E-field distribution near regions A and B, respectively.

3) OPTIMIZATION OF FGM CABLE JOINTS

To develop FGM joints with improved E-field distribution, proper optimization methods are required [7]. In this study, an iterative optimization approach shown in Fig. 10 was applied. The initial permittivity or conductivity of the SiR insulation was uniformly set to $\varepsilon_{\min}$ or $\sigma_{\min}$. The ending conditions contains whether the maximum iteration steps are reached and whether the difference between subsequent E-field distributions is less than the error value. During the optimization process, spatial distributions of permittivity or conductivity were updated according to the E-field calculation results in previous iteration steps.

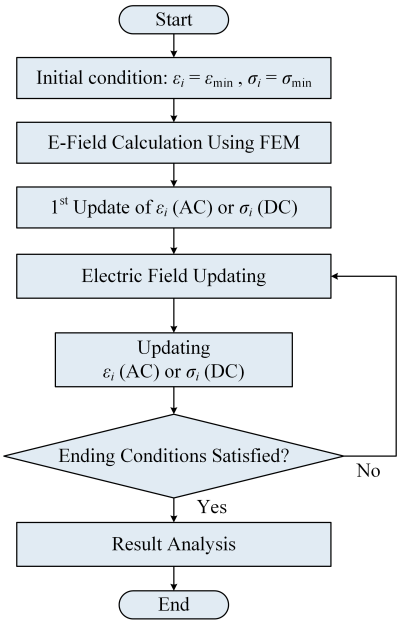

FIGURE 10. Flow chart of the optimization process in the FGM joints.

The updating method (i.e., optimization algorithm) of permittivity or conductivity distribution in FGM joints should be carefully considered since conventional algorithms (e.g., genetic optimization and particle swarm optimization) show some limitations in low calculation efficiency and inadequate convergence performance.

In this study, Okubo's algorithm [19] was used for the multilayer FGM joints This method has been employed by several researchers, such as Li *et al.* and Taalat *et al.* [19], [20], indicating its good applicability in the optimization of multilayer FGM insulation. Details of the design method in multilayer ε-FGM and σ-FGM joints are described in our previous publications [10]. It should be noted that the number of layers set to 20 because fewer layers ($N < 10$) lead to inadequate performance in electric field regulation, whereas an excessively high layer number ($N > 50$) may significantly reduce the efficiency of the FEM calculation.

For pointwise FGM joints, the topology optimization method is utilized. This approach originates from the design of advanced mechanical structures, where high stiffness, high strength, and low weight are required [21]. Recently, Li *et al.* [11] used topology optimization in a permittivity graded solid insulator and verified its effectiveness in the FGM insulation, especially in the pointwise FGM. To employ topology optimization, a proper design problem should first be developed. In the FGM cable joints, the graded SiR insulation is utilized to 1) uniformly distribute the electric field and 2) relieve the local electric field distribution in regions A and B. Therefore, the design problem can be expressed as

$$\begin{aligned} &\text{find } \varepsilon\,(r,z) \in \Omega_1 \ \text{ or } \ \sigma\,(r,z) \in \Omega_2 \\ &\min\ f = w \cdot f_{\mathrm{a}} + (1-w) \cdot \left(\frac{f_{\mathrm{b}} + f_{\mathrm{c}}}{2}\right) \\ &s.t.\ \varepsilon_{\min} \le \varepsilon\,(r,z) \le \varepsilon_{\max} \ \text{ or } \sigma_{\min} \le \sigma\,(r,z) \le \sigma_{\max} \end{aligned} \quad (1)$$

where $\varepsilon(r, z)$ or $\sigma(r, z)$ represent permittivity or conductivity distribution (Fig. 8c and 8e) Ω_1 and Ω_2 represents the area of graded permittivity in Fig. 8c and graded conductivity in Fig. 8e. The objective function f represents the status of E-field distribution, including three different subobjectives

$$f_{\mathrm{a}} = \frac{1}{C_0}\int_{\Omega_2} |E - E_{\mathrm{mean}}|^2\, d\Omega, \quad f_{\mathrm{b}} = \frac{E_{\mathrm{A}}}{E_{\mathrm{A0}}}, \quad f_{\mathrm{c}} = \frac{E_{\mathrm{B}}}{E_{\mathrm{B0}}} \quad (2)$$

The 1st subobjective f_{a} is a characterization of E-field uniformity. A smaller f_{a} means that the magnitude of the electric field is closer to the mean E-field E_{mean}, which is derived from the voltage of the inner conductor V_{cond} and the radial thickness of the joint insulation D, i.e., $E_{\mathrm{mean}} = V_{\mathrm{cond}}/D$. The variable C_{ref} is to normalize the initial value of f_{a} to 1. The other two subobjectives (f_{b} and f_{c}) are used to minimize the local E-field intensification. E_{A} and E_{B} are the magnitudes of E-field near region A and B. E_{A0} and E_{B0} are initial E_{A} and E_{B} values in the uniform joint. Obviously, a smaller f_{b} or f_{c} indicates a lower degree of E-field distortion. To balance these subobjectives in f, a weighting coefficient w is included, which is set to 0.5 in this study.

As for the updating algorithm, the global convergence method of moving asymptotes (GCMMA) was used. GCMMA converts the high-dimensional design problem into a series of explicit convex subproblems, significantly increasing the numerical efficiency. More details of the topology optimization method can be found in [11].

B. OPTIMIZATION RESULTS OF MULTI-LAYER FGM

1) SPATIAL DISTRIBUTION OF PERMITTIVITY AND CONDUCTIVITY

The radial distributions of permittivity in the multilayer ε-FGM and conductivity in the multilayer σ-FGM are illustrated in Fig. 11. In the multilayer ε-FGM, the permittivity in the 1st layer rises to $\varepsilon_{\max}$ after optimization, but remains to be $\varepsilon_{\min}$ in the other layers. For the multilayer σ-FGM, the conductivity distribution shows a similar pattern t in FGM-0.1CNT and FGM-0.2CNT. With a higher $\sigma_{\max}$, some "buffer layers" with medium conductivity occur between the high σ layer and low σ layers.

The change in the distribution patterns in conductivity is related to the variation range of the dielectric properties.

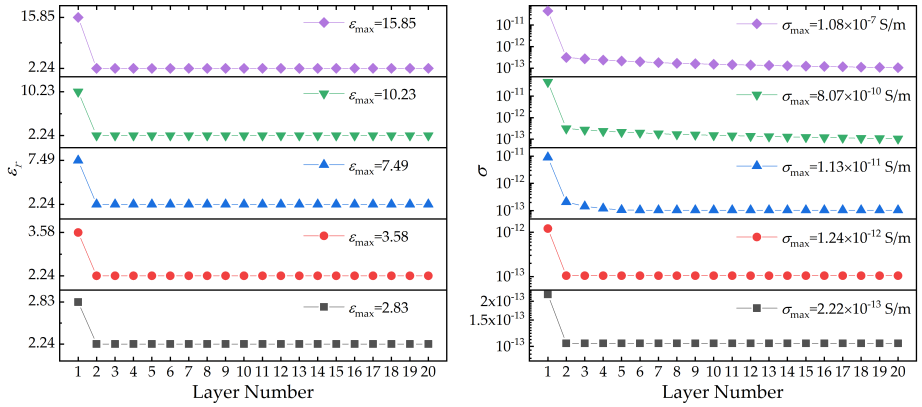

(a) Multi-layer ε-FGM (b) Multi-layer σ-FGM

FIGURE 11. Radial distribution of dielectric properties in multilayer FGM joints.

From Fig. 5, we can see that with an increase in the MWCNT doping ratio, the increase in conductivity is much larger than that in permittivity. For instance, in the FGM-0.3CNT material, the variation range of permittivity $R_{eps} = \varepsilon_{max}/\varepsilon_{min} = 3.34$, while the variation range of conductivity $R_{cond} = \sigma_{max}/\sigma_{min} = 107.62$. Our previous research indicated that when R_{eps} or R_{cond} was above 100, the aforementioned buffer layers were arranged in the multilayer FGM joints (see Fig. 5b-5e in [10]). The existence of buffer layers can relieve interfacial E-field intensification between high ε/high σ and low ε/low σ layers, which is a major reason for the abnormal deterioration in the electrical withstanding performance of the FGM insulators [22].

It should be noted that when the upper limit of the dielectric constant is not high enough (e.g., less than 10), the gradients of permittivity or conductivity can be trivial (Fig. 11). This is because the FGM structure is mainly used to alleviate the concentration of the electric field distribution. For the places where the E-field distribution is originally more uniform, it is not urgent to rise the permittivity or conductivity. Therefore, it is inevitable that there are multiple layers of the same dielectric constant in Fig. 11, and the value of the dielectric constant is the minimum value of the dielectric constant of the FGM material system.

2) ELECTRIC FIELD DISTRIBUTION

The electric field distributions of the uniform and multilayer FGM cable joints are illustrated in Fig. 12. In the uniform joint, the electric field is strongly intensified in the vicinity of points A and B under AC voltage. When it changed from AC to DC, the E-field intensification at point A was relieved (Fig. 12b), whereas the E-field near point B was significantly increased (Fig. 12c) The above phenomenon is caused by the small radius of curvature of the metal connectors and semiconductive layers, as well as the large dielectric mismatch between the conductors and the insulation materials.

The E-field intensification can be relieved to some extent by the multilayer FGM joints. For the ε-FGM joints under AC voltage, the electric field near point B is reduced owing to the increased permittivity in layer 1, and a higher upper limit of permittivity ε_{max} leads to better performance in electric stress release. Nevertheless, the influence of the multilayer ε-FGM on the overall E-field distribution and local E-field at point A seems to be trivial. For the σ-FGM joints under DC voltage, it can be seen from Fig. 12a that the E-field intensification at point B is nearly eliminated in the FGM-0.3CNT, FGM-0.4CNT, and FGM-0.5CNT joints. Moreover, the existence of a buffer layer in the σ-FGM joints results in a more uniform interfacial E-field distribution than in the ε-FGM joints, as shown in Fig. 12c.

Quantitative results of the E-field distribution can be drawn from Fig. 13, which depicts the E-field stress along the cutting lines in Fig. 9. In the uniform joint, the maximum E-field stresses near points A and B (named E_A and E_B, respectively) are 10.61 kV/mm and 15.21 kV/mm, respectively, under AC voltage and change to 2.41 kV/mm and 32.78 kV/mm under DC voltage For the ε-FGM joints, the E-field regulation mainly occurs inside layer 1. This leads to a monotonous reduction in E_A and E_B with an increase in ε_{max}. Specifically, E_A is decreased from 10.61 kV/mm to 7.05 kV/mm (reduced by 33%), and E_B is decreased from 15.19 kV/mm to 8.72 kV/mm (reduced by 43%).

For the σ-FGM joints under DC voltage, strong E-field enhancement at point B is largely relieved. In detail, E_B decreases from 32.78 kV/mm to 3.44 kV/mm (reduced by 89%). Simultaneously, at point A, E_A first decreases from 2.41 kV/mm to 1.24 kV/mm when σ_{max} increases to 1.13×10^{-11} S/m (the value of FGM-0.3CNT) and then bounces back to 2.18 kV/mm when σ_{max} further increases to 1.08×10^{-7} S/m (the value of FGM-0.5CNT). Nevertheless, the E_A in FGM-0.5CNT is still lower than that of a uniform joint. These results verify the effectiveness of optimized multilayer FGM for E-field regulation in cable joints.

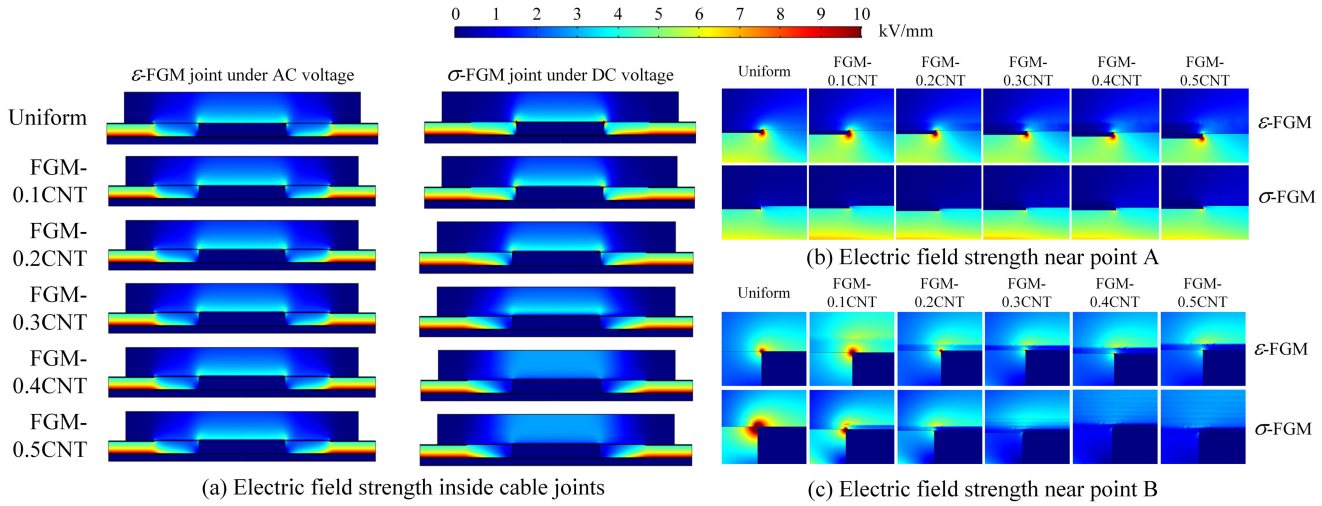

FIGURE 12. E-field contours of the uniform and multilayer FGM joints.

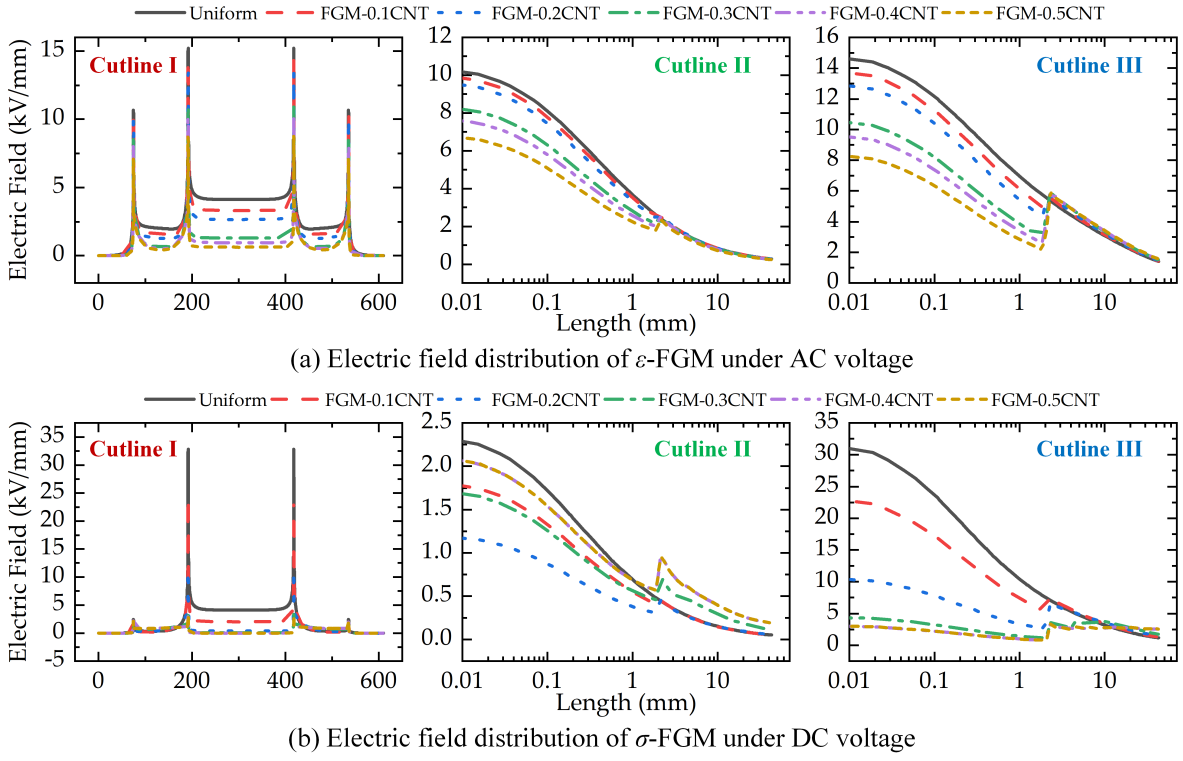

FIGURE 13. E-field distribution along the cutting lines in the uniform and multilayer FGM joints.

C. OPTIMIZATION RESULTS OF POINTWISE FGM

1) SPATIAL DISTRIBUTION OF PERMITTIVITY AND CONDUCTIVITY

Fig. 14 illustrates the spatial distribution of the dielectric properties in the topology-optimized ε-FGM and σ-FGM. The optimal distribution patterns of the permittivity and conductivity show some similarities to each other. For instance, high ε and high σ materials occupy similar places, that is, around the outer semiconductive layer (region A) and the metal connector (region B). In addition, the high permittivity area exhibits a "dual hump" shape in the middle of the joint and a "horn" shape near the tip points of the outer semiconductive layer.

The similarities between permittivity and conductivity distribution can be attributed to the identical format of Maxwell equations under AC and DC conditions [10]. Nevertheless,

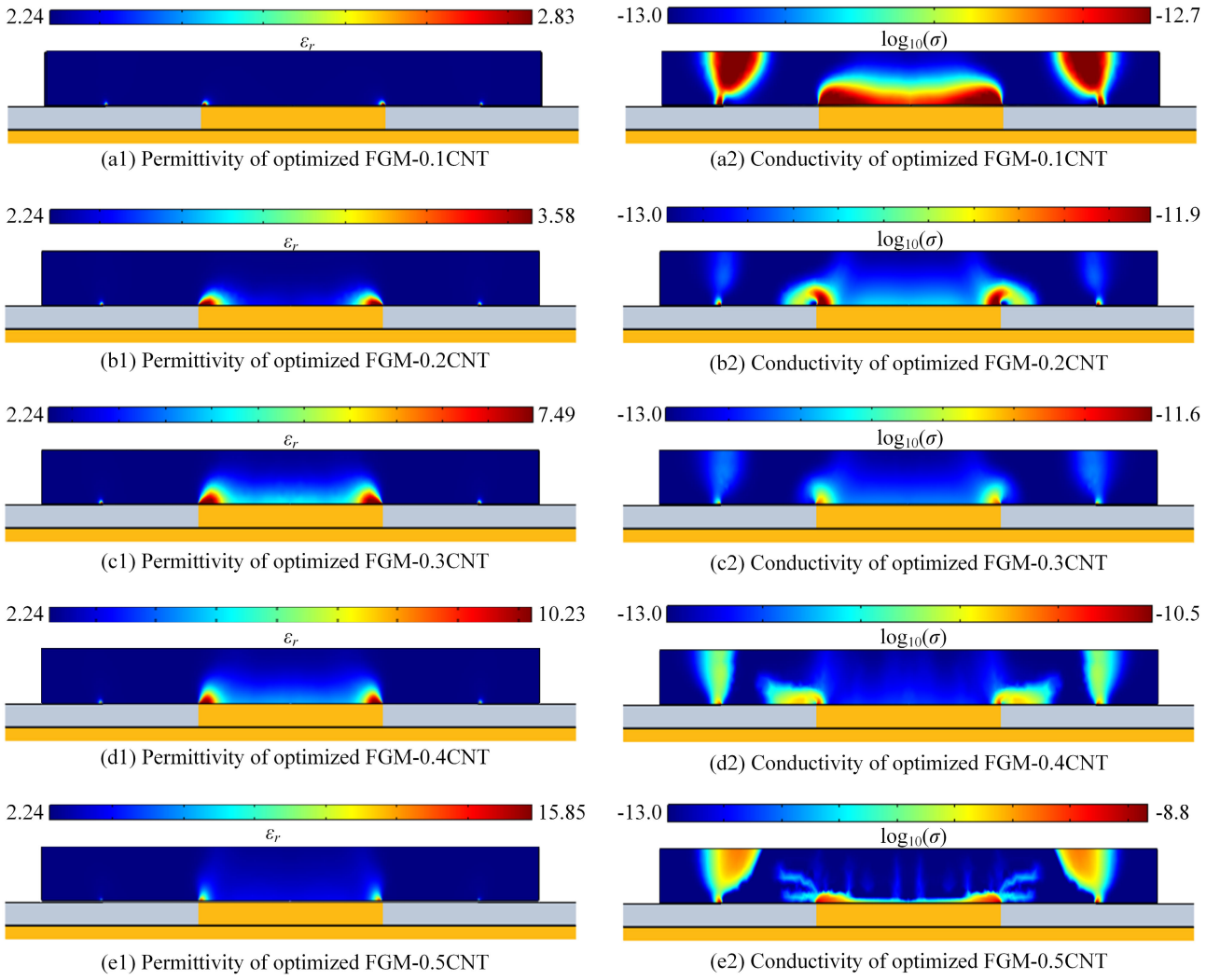

FIGURE 14. Two-dimensional distribution of dielectric properties in the pointwise FGM joints, including (a) FGM-0.1CNT, (b) FGM-0.2CNT, (c) FGM-0.3CNT, (d) FGM-0.4CNT, and (e) FGM-0.5CNT. Note that the conductivity distribution is on a logarithmic scale.

some differences in the distribution patterns still occur. For instance, the area of the high σ region in the σ-FGM is much larger than that in the high ε region in the ε-FGM. This can be caused by the differences in the E-field distribution in the uniform joints, that is, initial conditions before the topology optimization.

2) ELECTRIC FIELD DISTRIBUTION

Compared to the multilayer FGM joints, the pointwise FGM joints exhibit better performance in the E-field regulation (Fig. 15). Under AC voltage, a more uniform overall distribution of the E-field is established in the pointwise ε-FGM than in the multilayer ε-FGM in Fig. 12a. In addition, the local E-field distribution near point B is decreased to less than 5 kV/mm when FGM-0.5CNT is utilized (Fig. 15c).

Under DC voltage, the effect of the E-field optimization is also obvious; that is, E_B decreases to less than 2 kV/mm in the FGM-0.5CNT joint. It should be noted that a ''trade-off'' phenomenon occurs during the topology optimization process. In other words, decreasing the E-field at point B may lead to an increase in the E-field in adjacent areas. Despite this trade-off phenomenon, the uniformity of the E-field distribution in both the ε-FGM and σ-FGM joints is still much better than that of the uniform joint, indicating the effectiveness of topology-optimized FGM joints.

The E-field distribution along the aforementioned cutting lines is shown in Fig. 16, which also shows that the pointwise FGM joints have better performance than the multilayer FGM. For the ε-FGM joints (Fig. 16a), E_A is decreased from 10.61 kV/mm to 1.49 kV/mm (reduced by 86%), and E_B is decreased from 15.21 kV/mm to 1.71 kV/mm (reduced by 89%). Another interesting phenomenon is that when the amount of CNT doping increases to 0.4wt% and 0.5wt% the position of the maximum electric field in the cutting line II and III can shift from points A or B to the middle of the cutting lines.

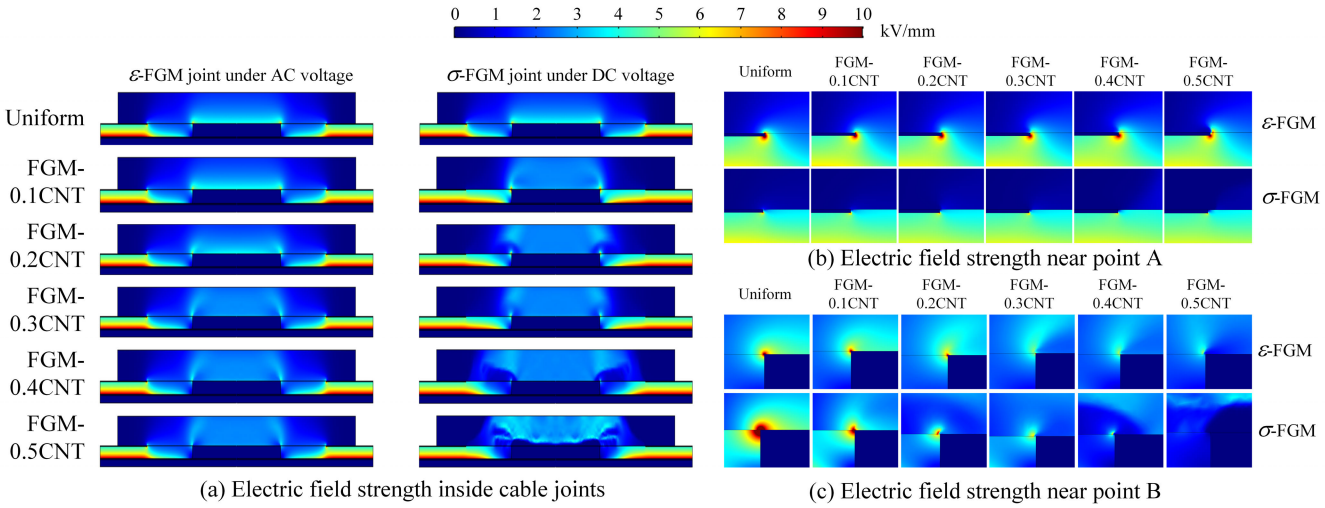

FIGURE 15. E-field contours of the uniform and pointwise FGM joints.

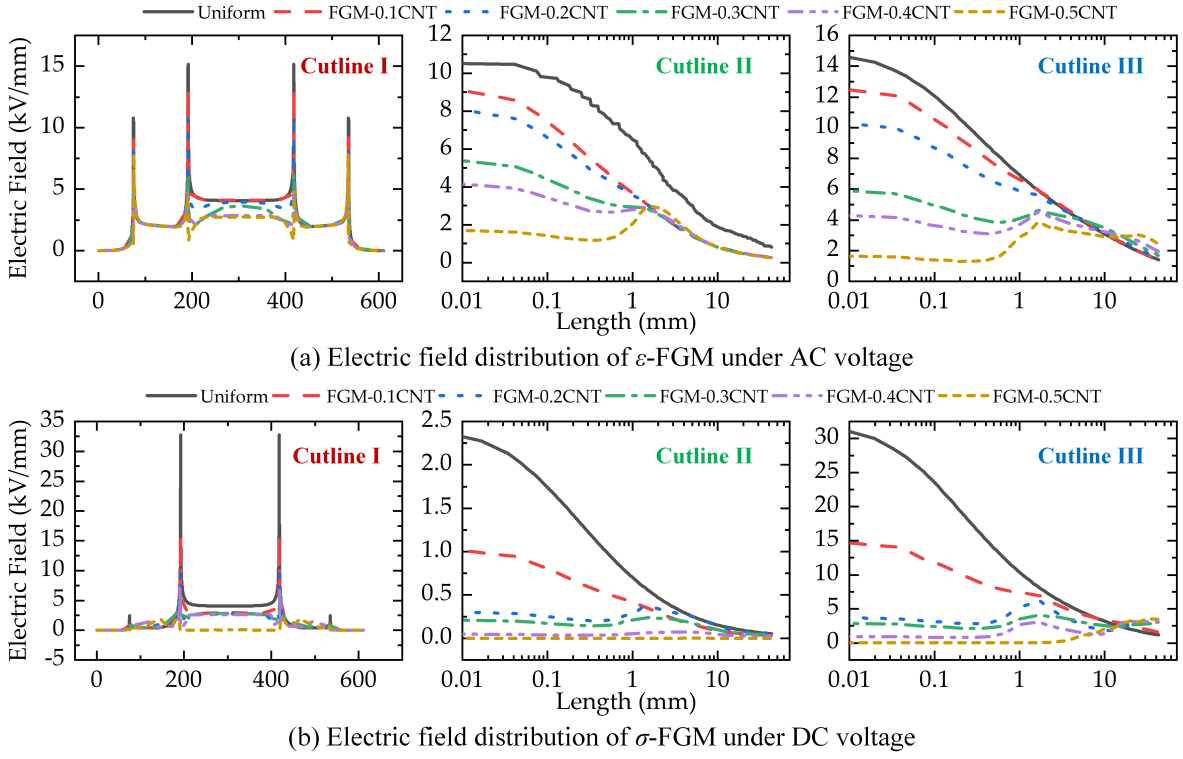

FIGURE 16. E-field distribution along the cutting lines in the uniform and pointwise FGM joints.

For the σ-FGM joints, E_A is decreased from 2.41 kV/mm to 0.05 kV/mm (reduced by 98%), and E_B is decreased from 32.78 kV/mm to 0.03 kV/mm (reduced by 99%). In the FGM-0.5CNT joints under DC voltage, the E-field strength along cutting lines II and III becomes almost uniform. Compared to the multilayer FGM joints (Fig. 13), the topology-optimized pointwise joints have better E-field uniformity and further decreased E-field strength along the concerned cutting lines, indicating better E-field optimization performance.

IV. DISCUSSION

From Section 3, we can see that the E-field at points A and B is significantly reduced with the application of the FGM joints. However, a relatively high E-field area occurs in the middle part of the joint insulation, which is especially

TABLE 3. Electric field parameters in the uniform and FGM joint insulation.

Voltage	Joint Name	FGM Type	E_A*	E_B*	E_{max}*	η**
AC	Uniform		10.61	15.21	15.21	0.17
	FGM-0.1CNT	Multilayer	10.28	14.28	14.28	0.18
		Pointwise	8.00	12.99	12.99	0.20
	FGM-0.2CNT	Multilayer	9.93	13.44	13.44	0.19
		Pointwise	7.06	10.72	10.72	0.24
	FGM-0.3CNT	Multilayer	8.61	11.01	11.01	0.23
		Pointwise	4.68	6.19	6.19	0.41
	FGM-0.4CNT	Multilayer	7.97	10.04	10.04	0.25
		Pointwise	3.60	4.52	6.43	0.40
	FGM-0.5CNT	Multilayer	7.05	8.72	8.72	0.29
		Pointwise	1.50	3.81	7.85	0.32
DC	Uniform		2.41	32.78	32.78	0.08
	FGM-0.1CNT	Multilayer	1.87	24.05	24.05	0.11
		Pointwise	1.05	15.51	15.51	0.16
	FGM-0.2CNT	Multilayer	1.24	10.99	10.99	0.23
		Pointwise	0.37	3.85	9.64	0.26
	FGM-0.3CNT	Multilayer	1.78	4.59	4.59	0.56
		Pointwise	0.24	3.01	7.00	0.36
	FGM-0.4CNT	Multilayer	2.18	3.15	3.44	0.74
		Pointwise	0.08	1.00	7.30	0.35
	FGM-0.5CNT	Multilayer	2.18	3.15	3.44	0.74
		Pointwise	0.05	0.03	3.52	0.72

* Unit: kV/mm.

** E_{mean} = 2.55 kV/mm

obvious in the topology-optimized pointwise FGM joints (see Fig. 15a). Therefore, it is insufficient to evaluate the E-field regulation performance by merely E_A and E_B, as points A and B may no longer be the place of the maximum E-field in the optimized FGM joints. To solve this problem, the E-field utilization factor η is employed, which is expressed in Equation (3):

$$\eta = \frac{E_{mean}}{E_{max}} \tag{3}$$

where E_{mean} is identical to the value in Equation (2), and E_{max} represents the maximum E-field inside the entire joint insulation. Obviously, a higher value of η indicates better E-field uniformity. Table 3 lists the E-field parameters in the uniform and different FGM joints depicted in Fig. 17.

From the above E-field parameters, we can see that the σ-FGM joints generally have lower E_{max} and higher η than the ε-FGM joints, indicating better performance in the E-field regulation. This can be attributed to a much larger variation range of conductivity than permittivity when the MWCNT filler was doped. Previously, several researchers and our team [10], [23], [24] verified that in the FGM insulation, a larger variation range in permittivity or conductivity leads to a better performance in E-field control, including lower E_{max} and better E-field uniformity. However, the use of the FGM-0.5CNT joints for cable insulation is very challenging. The following problems may exist.

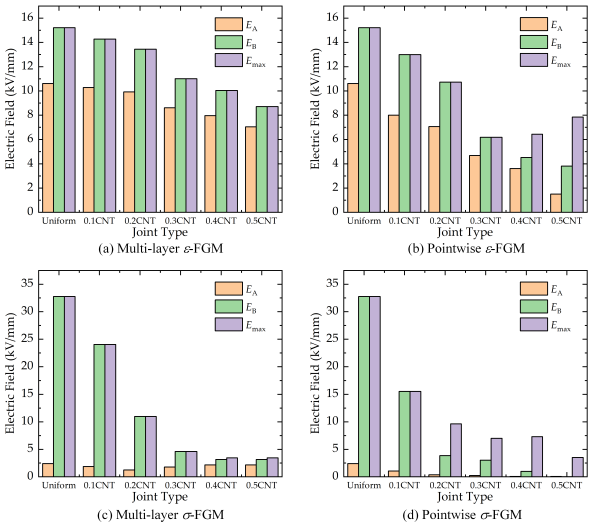

FIGURE 17. E-field parameters of the uniform and FGM joints.

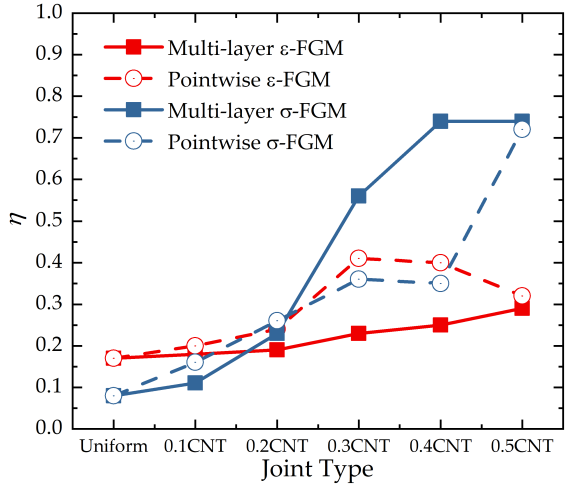

FIGURE 18. E-field utilization factor of the uniform and FGM joints.

(1) From Fig. 5, we can see that the SiR-0.5CNT material has a high dielectric loss (tanδ close to 0.1) and very low breakdown strength (E_b < 2 kV/mm), which can induce thermal and electrical breakdown in practical usage.

(2) The mechanical performance is also degraded in the SiR-0.5CNT material (shown in Fig. 6), increasing the probability of cracking during installation and operation.

(3) The fabrication of the FGM-0.5CNT joints is difficult, considering the complex structure of the high-conductivity area shown in Fig. 14e2.

(4) In the FGM-0.3CNT, FGM-0.4CNT, and FGM-0.5CNT joints, the E-field regulation performance is saturated or even degraded with a higher MWCNT loading ratio, which is indicated by the unchanged or even increased E_{max} (Fig. 17c-d and Fig. 18)

In summary, the FGM-0.5CNT joints (and FGM-0.4CNT joints) are not practically suitable owing to their poor

insulation properties, degraded mechanical performance, difficult fabrication process, and saturation in the E-field regulation. When comprehensive consideration is taken, the FGM-0.3CNT joint is preferred because of its relatively low dielectric loss (tanδ $<$ 0.01), and the breakdown strength of the material used is Eb $>$ 10 kV/mm. Judging from the electric field distribution inside the FGM structure (shown in Fig. 13 and Fig. 16), it basically meets its insulation requirements. In addition, it has unaffected mechanical performance (Fig. 6), and relatively simple structure (Fig. 14c1-c2). The FGM-0.3CNT joint still has adequate performance in E-field regulation (η rises from 0.08-0.17 to 0.23-0.56), indicating its applicability in advanced power cable joints.

V. CONCLUSION

To investigate the applicability of functionally graded materials (FGMs) in power cable joint insulation, the material feasibility and design method of the FGM joints was investigated, which was realized by an experimental study on silicone rubber (SiR)/multiwall carbon nanotube (MWCNT) nanocomposites and a simulation study on the multilayer and pointwise FGM joints.

The following conclusions were drawn:

1) In the SiR/MWCNT nanocomposites, a very low content of the MWCNTs (no greater than 0.5 wt%) can significantly improve the relative permittivity (from 2.24 to 15.85) and electric conductivity (from 1.05×10^{-13} to 1.08×10^{-7} S/m) of the insulation material, which is advantageous for E-field regulation. However, high dielectric loss, low breakdown strength and poor mechanical properties restrict the applicability of highly loaded (>0.3 wt%) SiR/MWCNT materials in actual power cable joints.

2) The results of the optimized FGM joints (both multilayer and pointwise) indicate their promising ability in E-field regulation. This is shown by the mitigation or even elimination of the E-field intensification at the tip points of the outer semiconductive layer (point A) and metal connector (point B). Furthermore, utilizing the FGM joints can decrease the maximum E-field and increase the E-field utilization factor, indicating better E-field uniformity.

3) When a comprehensive perspective is taken, the FGM-0.3CNT joints become the most practical candidate owing to their E-field regulation performance (η rises from 0.08-0.17 to 0.23-0.56), relatively low dielectric loss (tanδ $<$ 0.01), adequate breakdown strength (E_b $>$ 10 kV/mm), unaffected mechanical performance, and relatively simple structure. Furthermore, FGM-0.3CNT exhibits better performance under DC voltage, which implies that the FGM joints can be an effective approach in novel HVDC power cable system.

Despite the design process, fabrication of such FGM joints can also be an interesting topic, possible methods include inserting a buffer region with medium permittivity and/or conductivity to create a three-region cable joints shown in Fig. 22. Moreover, the effect of temperature on the design process of FGM insulation should also be investigated, especially for DC applications. Additionally, some different modeling techniques, such as controlling the maximum E-field to be less than BDE rather than increasing the E-field uniformity as high as possible, can be investigated to achieve different FGM joints with probably simpler gradient structure.

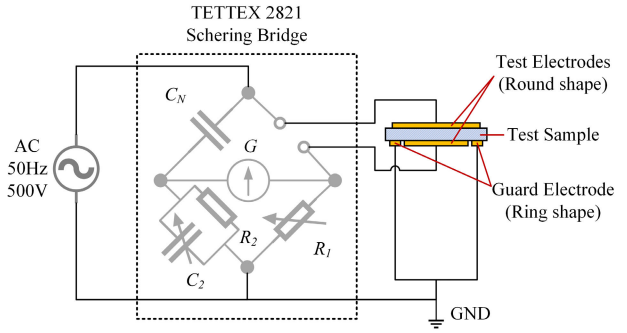

FIGURE 19. Experimental setup of permittivity and dielectric loss measurement.

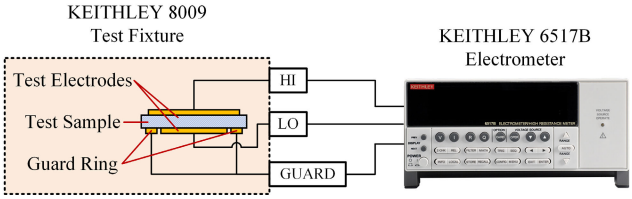

FIGURE 20. Experimental setup of conductivity measurement.

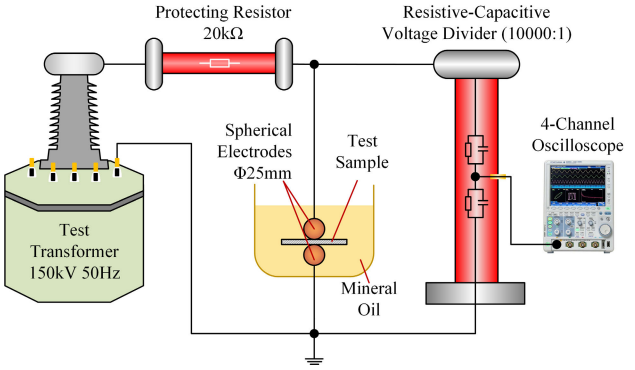

FIGURE 21. Experimental setup of AC breakdown strength test.

APPENDIX

The appendixes including the following contents.

1) Experimental setup of permittivity and dielectric loss measurement shown in Fig. 19, where a Schering bridge is utilized. C_N and R_2 are high-precision capacitor and resistor, respectively. C_2 and R_1 are variable passive components G is a galvanometer. According to IEC60250, a three-electrode configuration including two test electrodes and a guard ring was applied to reduce the influence of surface dissipation.

2) Experimental setup of conductivity measurement shown in Fig. 20. A Keithley 6517B electrometer and an 8009 conductivity test fixture were applied, which is compatible to the

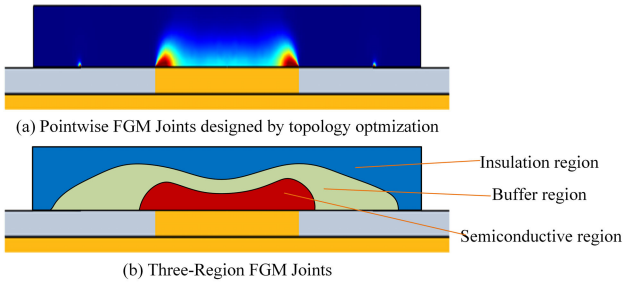

FIGURE 22. Three-region FGM joints derived from topology-optimized pointwise FGM joints applicable to the injection molding process.

test requirements in ASTM D257. Similar to the permittivity and dielectric loss test system in Fig. 19, a three-electrode system is utilized to eliminate the influence of surface current.

3) Experimental setup of AC breakdown strength test shown in Fig. 21. The test system was built According to IEC 60243. During the test procedures. The test sample was placed between two spherical electrodes (brass material, 25 mm diameter) and then immersed in transformer oil (Karamay 25) to inhibit surface flashover. The test voltage was increased continuously (rising rate 1 kV/s) until breakdown occurs.

4) Three-region FGM joints derived from topology-optimized pointwise FGM joints applicable to the injection molding process, shown in Fig. 22.

ACKNOWLEDGMENT

The authors would like to thank Dr. Wendong Li for the discussions and help with the topology optimization method, and to thank AJE (www.aje.com) for English editing service.

REFERENCES

[1] G. Mazzanti, J. Castellon, G. Chen, J. C. Fothergill, M. Fu, N. Hozumi, J. H. Lee, J. Li, M. Marzinotto, F. Mauseth, P. Morshuis, C. Reed, I. Troia, A. Tzimas, and K. Wu, "The insulation of HVDC extruded cable system joints. Part 1: Review of materials, design and testing procedures," *IEEE Trans. Dielectr. Electr. Insul.*, vol. 26, no. 3, pp. 964–972, Jun. 2019.

[2] P.-Y. Wang, H. Ma, G. Liu, Z.-Z. Han, D.-M. Guo, T. Xu, and L.-Y. Kang, "Dynamic thermal analysis of high-voltage power cable insulation for cable dynamic thermal rating," *IEEE Access*, vol. 7, pp. 56095–56106, 2019.

[3] R. Benato, A. Chiarelli, and S. D. Sessa, "Reliability assessment of a multi-state HVDC system by combining Markov and matrix-based methods," *Energies*, vol. 14, no. 11, p. 3097, May 2021.

[4] M. Zhu, Y. Gao, J. Chen, J. Li, Q. Yu, and C. Li, "Effect of XLPE/EPDM interface on space charge behavior in cable accessory," *IEEE Access*, vol. 7, pp. 183554–183564, 2019.

[5] B. X. Du, J. G. Su, and T. Han, "Temperature-dependent electrical tree in silicone rubber under repetitive pulse voltage," *IEEE Trans. Dielectr. Electr. Insul.*, vol. 24, no. 4, pp. 2291–2298, Aug. 2017.

[6] J. Su, B. Du, J. Li, and Z. Li, "Electrical tree degradation in high-voltage cable insulation: Progress and challenges," *High Voltage*, vol. 5, no. 4, pp. 353–364, Aug. 2020.

[7] J. Li, H. Liang, Y. Chen, and B. Du, "Promising functional graded materials for compact gaseous insulated switchgears/pipelines," *High Voltage*, vol. 5, no. 3, pp. 231–240, Jun. 2020.

[8] G. Zhang, W. Li, Z. Liu, G. Su, B. Song, R. Xie, and J. Deng, "Research progress on dielectric functionally graded materials for electrical insulation," *Zhongguo Dianji Gongcheng Xuebao/Chin. Soc. Electr. Eng.*, vol. 37, no. 14, pp. 4232–4245, 2017.

[9] K. Kato, M. Kurimoto, H. Shumiya, H. Adachi, S. Sakuma, and H. Okubo, "Application of functionally graded material for solid insulator in gaseous insulation system," *IEEE Trans. Dielectr. Electr. Insul.*, vol. 13, no. 2, pp. 362–372, Apr. 2006.

[10] Y.-F. Zhang, M.-L. Fu, B. Luo, B.-J. Hui, S. Hou, Y.-J. Nie, F.-S. Zhou, and B. Feng, "Simulation of functionally graded material (FGM) for cable joint in AC and DC field optimization," in *Proc. IEEE Int. Conf. High Voltage Eng. Appl. (ICHVE)*, Sep. 2020, pp. 1–4.

[11] W.-D. Li, X.-R. Li, B.-H. Guo, C. Wang, Z. Liu, and G.-J. Zhang, "Topology optimization of truncated cone insulator with graded permittivity using variable density method," *IEEE Trans. Dielectr. Electr. Insul.*, vol. 26, no. 1, pp. 1–9, Feb. 2019.

[12] H. Jiang, X. Zhang, J. Gao, and N. Guo, "Dielectric and AC breakdown properties of SiO_2/MMT/LDPE micro-nano composites," *Energies*, vol. 14, no. 5, p. 1235, Feb. 2021.

[13] C.-W. Nan, Y. Shen, and J. Ma, "Physical properties of composites near percolation," *Annu. Rev. Mater. Res.*, vol. 40, no. 40, pp. 131–151, Aug. 2010.

[14] J. H. Kim, S. Lee, M. Wajahat, H. Jeong, W. S. Chang, H. J. Jeong, J.-R. Yang, J. T. Kim, and S. K. Seol, "Three-dimensional printing of highly conductive carbon nanotube microarchitectures with fluid ink," *ACS Nano*, vol. 10, no. 9, pp. 8879–8887, Sep. 2016.

[15] X. Huang, L. Xie, K. Yang, C. Wu, P. Jiang, S. Li, S. Wu, K. Tatsumi, and T. Tanaka, "Role of interface in highly filled epoxy/$BaTiO_3$ nanocomposites. Part I-correlation between nanoparticle surface chemistry and nanocomposite dielectric property," *IEEE Trans. Dielectr. Electr. Insul.*, vol. 21, no. 2, pp. 467–479, Apr. 2014.

[16] K. Y. Lau, A. S. Vaughan, and G. Chen, "Nanodielectrics: Opportunities and challenges," *IEEE Elect. Insul. Mag.*, vol. 31, no. 4, pp. 45–54, Jul. 2015.

[17] S. Li, G. Yin, G. Chen, J. Li, S. Bai, L. Zhong, Y. Zhang, and Q. Lei, "Short-term breakdown and long-term failure in nanodielectrics: A review," *IEEE Trans. Dielectr. Electr. Insul.*, vol. 17, no. 5, pp. 1523–1535, Oct. 2010.

[18] Z.-M. Dang, J.-K. Yuan, J.-W. Zha, T. Zhou, S.-T. Li, and G.-H. Hu, "Fundamentals, processes and applications of high-permittivity polymer–matrix composites," *Prog. Mater. Sci.*, vol. 57, no. 4, pp. 660–723, May 2012.

[19] W.-D. Li, X.-Y. You, H.-B. Mu, J.-B. Deng, and G.-J. Zhang, "Numerical optimization and 3D-printing fabrication concept of high voltage FGM insulator," in *Proc. IEEE PES Asia–Pacific Power Energy Eng. Conf. (APPEEC)*, Brisbane, QLD, Australia, Nov. 2015, pp. 1–4.

[20] M. Talaat, A. El-Zein, and M. Amin, "Developed optimization technique used for the distribution of U-shaped permittivity for cone type spacer in GIS," *Electr. Power Syst. Res.*, vol. 163, pp. 754–766, Oct. 2018.

[21] O. Sigmund and K. Maute, "Topology optimization approaches," *Struct. Multidisciplinary Optim.*, vol. 48, no. 6, pp. 1031–1055, Dec. 2013.

[22] Q. Huang, S. Li, T. Zhang, F. Ni, and J. Li, "Improvement of surface flashover characteristics about 45° insulator configuration in vacuum by a new organic insulation structure," *IEEE Trans. Dielectr. Electr. Insul.*, vol. 18, no. 6, pp. 2115–2122, Dec. 2011.

[23] H. Okubo, H. Shumiya, M. Ito, and K. Kato, "Optimization techniques on permittivity distribution in permittivity graded solid insulators," in *Proc. IEEE Int. Symp. Electr. Insul.*, Toronto, ON, Canada, Jun. 2006, pp. 519–522.

[24] Z. Liu, W.-D. Li, Y.-B. Wang, G.-Q. Su, G.-J. Zhang, Y. Cao, and D.-C. Li, "Topology optimization and 3D-printing fabrication feasibility of high voltage FGM insulator," in *Proc. IEEE Int. Conf. High Voltage Eng. Appl. (ICHVE)*, Chengdu, China, Sep. 2016, pp. 1–4.

YIFAN ZHANG was born in Jiangsu, China, in 1992. He received the B.S. degree from Xi'an Jiaotong University, China, in 2013, and the M.S. degree from Nagoya University, Japan, in 2016. He is currently working with the Electric Power Research Institute, China Southern Power Grid, China. His research interests include advanced insulation materials and power cable condition assessment.

YONGJIE NIE was born in Gansu, China, in 1986. He received the B.Eng. and Ph.D. degrees from Xi'an Jiaotong University, China, in 2007 and 2018, respectively. He is currently working with the Electric Power Research Institute, Yunnan Power Grid Company Ltd. His research interests include insulating materials, surface flashover in vacuum, and surface modification.

BING LUO was born in Sichuan, China, in 1966. He received the B.S. degree from Huazhong University of Science and Technology, in 1987, the M.S. degree from Chongqing University, in 1990, and the Ph.D. degree from Tsinghua University, China, in 1996. He is currently a Senior Technical Expert and a Chief Engineer with the Department of High Voltage Technology, Electric Power Research Institute, China Southern Power Grid, Guangzhou, China. His research interests include high voltage insulation and detection technology.

MINGLI FU (Member, IEEE) was born in Shannxi, China, in 1962. He received the B.S. degree in electrical engineering from Xi'an Jiaotong University, China, in 1983, and the Ph.D. degree from the University of Southampton. He spent many years with China Electric Power Research Institute (CEPRI), as a Research and Development Engineer, a Senior Engineer, and the Group Head, before he moved to the U.K., as a Visiting Research Fellow with the University of Southampton, in 1997. Then, he worked at U.K. universities and Industry Research and Development Sector, as a Postdoctoral Research Fellow, a Lecturer, and a Technology Consultant. He joined the Electric Power Research Institute, China Southern Power Grid, as a Senior Expert, in 2013. He is currently leading a team working on innovative technologies of HVDC/HVAC insulation, safe system operation, and asset management.

SHUAI HOU was born in Heilongjiang, China, in 1988. She received the B.S. and M.S. degrees in electrical engineering from Harbin University of Science and Technology, Harbin, China, in 2010 and 2013, respectively. She is currently a Researcher with the Department of High Voltage Technology, Electric Power Research Institute, China Southern Power Grid, Guangzhou, China. She focuses on HVDC and HVAC cable technology and nonlinear insulation materials.

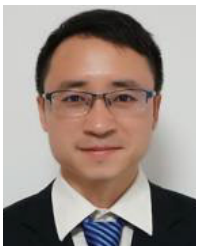

BAOJUN HUI was born in Shaanxi, China, in 1988. He received the B.S. and M.S. degrees from Xi'an Jiaotong University, China, in 2012 and 2015, respectively. He is currently working with the Electric Power Research Institute, China Southern Power Grid. He is mainly engaged in the research of power cable performance, partial discharge detection, and evaluation technologies.

XIANPING ZHAO was born in Yunnan, China, in 1974. He received the B.S. degree from Huazhong University of Science and Technology, in 1996, and the M.S. degree from Kunming University of Science and Technology, in 2009. He is currently working with the Electric Power Research Institute, Yunnan Power Grid Company Ltd. His research interests include testing technology and condition evaluation of high voltage power equipment.

BIN FENG was born in Shandong, China, in 1983. He received the B.S. degree in physics and the M.S. degree in electrical engineering from Xi'an Jiaotong University, in 2004 and 2007, respectively. After graduating, he joined Guangzhou Electric Power Design Institute, China Southern Power Grid Company Ltd., as an Engineer. In 2015, he joined the Electric Power Research Institute, China Southern Power Grid, as a Researcher. His research interests include overvoltage protection of power systems and cable insulation state evaluation.

WENBO ZHU was born in Harbin, China, in 1989. He received the B.S. and Ph.D. degrees in electrical engineering from Tianjin University, in 2012 and 2019, respectively. Since then, he has been with the Electric Power Research Institute, China Southern Power Grid, as a Researcher. His research interests include power equipment fault diagnosis and condition monitoring.